doi:10.1038/nature10089

Supplementary Methods

Regional summer temperature and temperature sensitivity

Average regional summer temperatures were calculated as the glacier area-averaged June, July and August surface air temperature from the National Centers for Environmental Prediction (NCEP) / National Center for Atmospheric Research (NCAR) Reanalysis 1 (R1)[31] for all land ice located in the CAA (Fig. 1). The same analysis was done for a merged European Centre for Medium-Range Weather Forecasts (ECMWF) ERA-40[32]/ Interim Reanalysis3[33] (ERA-40 prior to 1989 and ERA Interim after) and for 700 mb temperatures in both datasets. Glacier area-averaged summer temperatures are included in the Supplementary Data. All of our results indicate that 4 of the 5 warmest years since 1960 occurred after 2004 (1998 was also among the top 5 warmest years), but we do not attempt to characterize the uncertainty in these datasets. Between 1954 and 1960, R1 summer temperatures show a warming of similar magnitude as the post-2004 warming. Glacier temperature sensitivity was determined by regressing the error-weighted mean annual mass change of all three methods (SMB + *D*, ICESat, and GRACE) against glacier area averaged June, July and August ERA Interim surface air temperatures. ERA Interim surface air temperatures were used to keep the analysis independent of the R1, which is used to force the surface mass budget model. Similar analysis done with R1 temperatures or with error weighted mean annual mass changes that exclude SMB + *D* and all give sensitivities that are within ± 3 Gt yr^{-1} K^{-1} of the stated value.

Glacier outlines

Glacier outlines for the Northern CAA were compiled from three sources. Ice outlines for Axel Heiberg Island and the Prince of Wales, Manson and Sydkap Ice Caps were taken from the Global Land Ice Measurement from Space (GLIMS) dataset[34]. Ice outlines for the Devon Ice Cap were taken from Burgess and Sharp[35]. All remaining ice outlines were generated using a normalized-difference snow index (NDSI). Glacier outlines for the Southern CAA were taken from the National Snow and Ice Data Center's Circum-Arctic Map of Permafrost and Ground-Ice Conditions[36]. These outlines were used to determine the total glacier area for each region and are used in the SMB model and ICESat analysis. All ice outlines for the Northern CAA were

generated from 1999-2003 Landsat-7 (ETM+) imagery. Outlines for the Southern CAA are a digitized version of the original outlines delineated by the Canadian Glacier Inventory[37] from 1:250,000 scale National Topographic System (NTS) maps, compiled at 1:125,000 and based on the vertical air-photo coverage of the Arctic most likely in the late1950s and early 1960s. Between 1958-61 and 2000-2001 the glacier area of Bylot Island, the island just to the North of Baffin Island, decreased by about 5 % making the current glacier area of the Southern CAA slightly less than the areas used in this study[38]. This is supported by ICESat-derived elevation changes for the Southern CAA that clearly show that there has been a general shrinkage in glacier area since the delineation of the outlines. Overestimated glacier areas should not influence ICESat volume change calculations since elevation changes approach zero in places where glacier outlines erroneously encompass ice-free areas. However, care must be taken when volume or mass changes are converted into area-averaged changes. Glacier outlines are included in the Supplementary Data.

Digital Elevation Models (DEM)

The surface mass budget (SMB) modeling and ICESat analysis rely on DEMs to downscale R1 temperature fields and to extrapolate elevation changes, respectively. In order to retain independence between the two methods, two different DEMs are used: The SMB modeling uses a DEM of northern CAA which is assembled from 149 individual Canadian Digital Elevation Data (CDED) DEMs, while the ICESat analysis uses a DEM of 50 m resolution which is resampled from 321 tiles of the ASTER Global Digital Elevation Model, a product of NASA and METI. The CDED DEM is derived from 1:60,000 aerial photographs taken in the late 1950s and early 1960s. The ASTER GDEM is a compilation of stacked and cloud-filtered ASTER DEMs acquired since the year 2000. The CAA part of the GDEM has been controlled against the CDED DEM in order to replace data voids and outlier values, representing less than 1 % of the GDEM area. We validated the two DEMs over land and glacier surfaces using ICESat observations from fall 2003 (Supplementary Table 1). Based on this, the ASTER GDEM is adjusted for a mean bias of -14 m, while no correction is applied to the CDED DEM. A comparison of the glacier hypsometries from the two DEMs can be seen in Supplementary Fig. 5. The impact of the choice of DEMs on hypsometrically averaged ICESat elevation changes is negligible (< 0.01 m yr^{-1}).

Surface Mass Budget (SMB) Model

Melting of snow and ice is determined for each grid cell (i, j : 500 m by 500 m equal area grid) within the SMB model domain (Northern CAA: Fig. 1 and 3) for each day (k) using the temperature-index model described by Gardner and Sharp (2009)[39] with a modified melt water retention scheme. Here, the upper limit of meltwater and liquid precipitation that can be refrozen and or retained by the annual snowpack ($F_{MAX(i,j,k)}$ kg m^{-2}) is set equal to the cold content of the annual snow layer:

$$F_{MAX(i,j,k)} = \frac{c}{L} A_{(i,j,k)} T_{S(i,j,k)}$$

where c and L are the specific heat capacity (J kg^{-1} K^{-1}) and the latent heat of fusion of ice (J kg^{-1}), and $A_{(i,j,k)}$ is the annual accumulation per unit area (kg m^{-2} yr^{-1}). $T_{S(i,j,k)}$ is the initial snow temperature and is assumed to be equal to the mean annual 2 m air temperature. This approach assumes that all refreezing occurs within the annual snowpack. If there is sufficient melting to remove the entire snowpack then the refrozen water is allowed to melt at a later date as ice. If the entire snowpack is not removed, then the refrozen melt water and remaining snow are added to the mass of the glacier.

The SMB model is forced with bias-corrected R1 mean daily temperature and precipitation fields that are downscaled to the resolution of the SMB model. R1 daily air temperature fields for 700 mb and 850 mb are linearly interpolated to a fixed height of 2500 m. Temperature $T_{(i,j,k)}$ and precipitation $P_{(i,j,k)}$ fields are then remapped to the resolution of the SMB model using bilinear interpolation and corrected for biases using *in situ* observations (Supplementary Table 2 and Supplementary Table 3). This is done by determining differences between regridded R1 values and observations at each location of measurement and extrapolating these differences across the model domain using natural neighbor interpolation. Difference fields are then used to scale $P_{(i,j,k)}$ for biases in mean annual precipitation and to adjust $T_{(i,j,k)}$ for biases in monthly means and standard deviations. During the bias correction process the elevation field associated with $T_{(i,j,k)}$ (initially set to a constant 2500 m) is adjusted to match the elevations of the observations. To limit the geographic influence of the two coastal stations it was necessary

to prescribe observational temperatures at two additional locations during the bias correction process. Values over the Müller Ice Cap (79.8°N, -91.8°E) are set equal to those determined for the Prince of Wales Ice Field with an additional 1 ºC offset to better reproduce observed melt rates. Values over the Northern Ellesmere Ice Cap (81.9 °N, -75.9°E) are set equal to the temperatures observed over the Agassiz Ice Cap.

A 2 m air temperature field $T_{2m(i,j,k)}$ is then determined from $T_{(i,j,k)}$ using a modeled near-surface temperature lapse rate $\beta_{(i,j,k)}$ and a digital elevation model (DEM) of the glacier surface. $\beta_{(i,j,k)}$ is modeled as a linear function of $T_{a(i,j,k)}$ using the relationship proposed by Gardner and others (2009)[20], where $T_{a(i,j,k)}$ is a field containing the daily anomalies (1994-2005 climatology) in 3-day average R1 700 mb temperatures that have been remapped at the resolution of the SMB model using bilinear interpolation.

The model is run for the 60-year period from 1949 to 2009 using a Monte Carlo simulation with 1000 model realizations. For each model realization, values for free variables are assigned randomly from a normally distributed probability density function derived from previously published values (Supplementary Table 4). Additional mass flux terms resulting from melt/refreezing at the base of the glacier, avalanches, and blowing snow are neglected and assumed to be negligible. The annual regional SMB is determined by taking the average of the 1000 model realizations for the period from September 16th of the previous year to September 15th of the stated mass budget year. Annual surface mass budget results are provided in the Supplementary Data. To estimate the uncertainty in the modeled regional SMB we determine the measured SMB integrated over the basin of each glacier with a well-established measurement program (Agassiz Ice Cap, north western Devon Island Ice Cap, Meighen Ice Caps and White Glacier]. We then average the basin-integrated SMB values for each year and compare them with equivalent values generated using the SMB model. From this analysis we determine the standard error of the model with respect to the observations to be 140 kg m^{-2} yr^{-1} (Supplementary Fig. 6). The uncertainty in the regional SMB results (30 Gt yr^{-1}) is then taken to be two times this standard error multiplied by the total area of ice in the model domain (106,400 km^2).

In our simulations we do not account for changes in glacier elevation or area. For the 40 year period between 1960 to 2000, the glacier area of the Northern CAA is estimated to have shrunk by roughly 2 %[40]. We take this to be the upper bound of the possible change in area

between the acquisition of the ice outline (1999-2003) and the end of our study period (2009). Any reduction in ablation volume due to a decrease in surface area will be partly offset by an overall decrease in glacier elevations (-2.4 ± 0.5 m) that lead to slightly higher temperatures (0.02 °C) and more melt. To account for this possible source of error we apply a linearly increasing uncertainty of 0% at the start of our study increasing to 2% in 2009 to our model estimates of annual mass change.

ICESat

All available NASA ICESat/GLAS data from release 31 of the GLA06 altimetry product[12,21] are used in a joint analysis where surface slope and average elevation change (dh/dt) are estimated for planar rectangles that are fitted to 700 m long segments of near-repeat tracks[41]. The elevation residuals with respect to the least-squares plane solution are used to calculate annual elevation changes (dh) between consecutive ICESat observation campaigns covering the October/November time span. Repeat-track dh measurements between the fall of 2003 and the fall of 2009 are included in the Supplementary Data. The relation between annual dh and elevation is parameterized using third order polynomial fits for each glacier region. Annual volume changes (dV) are estimated by multiplying the polynomial fits by the hypsometric areas within 100 m elevation bins derived from the ASTER GDEM (Supplementary Fig. 5). More details about the methodology and error analysis can be found in Moholdt and others (2010)[22].

Glacier volume changes determined from ICESat are prone to several systematic errors due to crustal uplift, inter-campaign biases and uneven spatial sampling of elevation changes. Modeled glacial isostatic adjustment (GIA) in the CAA region indicate spatially variable uplift rates on the order of -1 to +7 mm yr^{-1} [42, 43]. When extracted over glacier surfaces, this yields average uplift rates of 4.2 ± 2.5 mm yr^{-1} for the Northern CAA and 3.0 ± 3.3 mm yr^{-1} for the Southern CAA (see GRACE section for more details on GIA). An additional elastic uplift due to increased present-day ice mass loss can also be expected[44]. A more significant source of error is the potential elevation biases between different ICESat laser campaigns. Inter-campaign biases of up to ±0.10 m yr^{-1} have been found over the Arctic Ocean by analyzing the time variation of the average mean sea-surface derived from ICESat[45]. When accounting for sea-level rise, the linear trend of the inter-campaign biases was estimated to be ~6 mm yr^{-1} for the period 2003-2007. Given the large uncertainty of crustal uplift and inter-campaign biases, and the relatively small impact they have on the overall CAA mass change (~0.5 Gt yr^{-1} and ~0.8 Gt yr^{-1} respectively), we

have chosen to not apply any bias corrections to the ICESat results but rather account for their uncertainty in our error estimates by adding random annual elevation change errors of ± 1.5 Gt yr^{-1} and ±10 Gt yr^{-1} respectively.

Spatial extrapolation of elevation changes that are required to derive volume changes can be an issue if observations are sparse or if there are large local variations in elevation change. Supplementary Fig. 5 shows the *dh/dt* variability and the amount of data within individual elevation bins. All major glacier basins are sampled by ICESat (Supplementary Fig. 7 and 8) but not all profiles are repeated each year, particularly in 2009 when the last laser failed one third of the way into the fall campaign. This means that ICESat results for 2009 are more susceptible to spatial sampling biases, especially in Southern CAA where profiles are more scattered. Such temporal variations in sampling are however accounted for in the error estimates, i.e. the mass budget error in 2009 is twice as high as in 2004. To test if variations in spatial sampling over different glacier types introduce biases in our regional extrapolation, we did separate calculations for tidewater and land-terminating glacier basins in Northern CAA (Supplementary Fig. 5). We found that the area-averaged elevation change rates of the two glacier basin types were not significantly different (Supplementary Table 5). The influence of subregional climatic variations and differences in spatial sampling was investigated by dividing the Northern CAA into 3 subregions and the Southern CAA into 2 subregions (Supplementary Fig. 1). The sum of subregional volume changes agrees well with the regional volume changes, indicating no significant bias due to uneven spatial sampling between the subregions (Supplementary Table 5). Alternative spatial extrapolation techniques using mean, median or higher order polynomial fits were also tested. We found little variation between these techniques with the exception of median methods, which are typically less negative due to a skewness of most elevation change histograms towards more negative values (Supplementary Table 5).

Conversion from *dV/dt* to mass change (*dM/dt*) is typically done by multiplying *dV/dt* by the density of ice (900 kg m^{-3} = 0.9 Gt km^{-3}), assuming a constant firn layer. For our study this assumption is likely not valid at elevations above the superimposed ice zone (~1200 m). In a warming climate, firn compaction will increase and more meltwater will be generated across the firn zone, some of which will contribute to mass loss through runoff and the remainder will percolate into the firn and refreeze. We therefore assign a density ratio that is less than that of ice for elevations above 1200 m assuming steady-state dynamics. The long response time of ice cap creep makes it unlikely that there have been widespread changes in glacier

emergence/submergence velocities in the interior regions of the ice masses. From field measurements of firn density collected on the Devon Island Ice Cap in the spring of 2004 and 2009 we estimate the plausible range of the density to be 0.66 ± 0.25 kg m^{-3} for elevations above 1200 m and 0.9 ± 0.01 kg m^{-3} for elevations below 1200 m. The high uncertainty of the firn density ratio has little impact on the overall results (only ±2 Gt yr^{-1}) since ~85 % of the total glacier volume loss occurs below 1200 m in both regions. The estimate of mass change is also relatively insensitive to the choice of firn line elevation; changing the firn line by ±100 m results in a change to our mass loss estimate on the order of ±1 Gt yr^{-1} when applied to the entire CAA.

GRACE

Here we use the GRACE observations (Mar. 2003 - Dec. 2009) of time-variable gravity provided by the Center for Space Research in its fourth release (CSR RL04). The GRACE data, based on "range-rate" measurements between the two satellites, are distributed as Stokes coefficients at monthly intervals up to spectral degree and order 60, which translates to a half-wavelength spatial resolution of approximately 300 km. Using elastic loading theory, the Stokes coefficients can be translated to maps of surface mass density anomalies[46]. At the shorter wavelengths, the GRACE coefficients are known to exhibit a strong correlation between coefficients of even and odd degrees l for constant order *m*, respectively, which shows up as North-South oriented stripes in the maps of surface mass density anomalies[47]. We correct the GRACE data for these inter-coefficient correlations following the method of Wouters and Schrama, 2007[48], where an empirical orthogonal function (EOF) decomposition is applied to the coefficients grouped by order *m* and EOF modes showing non-coherent temporal variability are filtered out. To suppress any remaining noise in the maps of monthly mass anomalies, the solutions are convolved with a Gaussian smoothing kernel with a 250-km half-width radius[29]. Due to the orbit characteristics of the GRACE satellites, a small number of coefficients are particularly sensitive to aliasing of high-frequency (intra-monthly) mass variations. These 'resonant' coefficients[24] (m = 8, 10 for l > 20; 15, 29, 31, 41; l >10 for l > m) show an unrealistically large variability[50, 51] and have been set to zero. The monthly GRACE data are accompanied by calibrated standard errors for each coefficient that are based on sub-set and inter-month comparisons. These are the errors on which we base the uncertainty of the monthly surface mass anomaly estimates. The GRACE satellites do not capture the degree-1 coefficients, related to the displacement of the Earth's center of mass, therefore, a geocenter model is included[52]. The original, poorly observed coefficients are replaced by values derived from satellite laser ranging[53].

The mass changes in the CAA are recovered following the method of Wouters and others (2008)[29]. The CAA and surrounding regions are separated into basins to which an initial mass anomaly is prescribed (Supplementary Fig. 1). The resulting field is converted to pseudo-GRACE observations and compared to the actual GRACE observations. In an iterative process, the mass anomalies in the basins are adjusted until an optimal agreement in a least-square sense is reached with the GRACE observations. In contrast to Wouters and others (2008)[29], no a-proir information is used in the initialization and the iterative process is started from zero anomalies, making our GRACE estimates fully independent of the ICESat and SMB model results. The dependence of the iterative process on the starting conditions was tested by initializing the process with random anomalies (in the range of -500 to +500 Gt) and identical results were obtained.

The mass changes observed by the GRACE satellites are the integral sum of various components (atmosphere, ocean, terrestrial water storage and cryosphere) and a number of corrections are therefore required before the ice mass variations can be isolated. The GRACE science teams remove atmospheric mass fluctuations using the 6-hourly pressure fields from the ECMWF operational analysis[54]. We compared the ECMWF fields to reanalysis fields from the National Centers for Environmental Prediction (NCEP)[55] and found that over the Northern CAA, differences between the two data sets introduce a negligible uncertainty of 0.3 ± 0.1 Gt yr^{-1}. No significant differences were found over Southern CAA (0.1 ± 0.1 Gt yr^{-1}). Glacial isostatic adjustment (GIA), the Earth's ongoing visco-elastic response to changing glacial loading, has been corrected for using a modified version of the widely adopted ICE-5G (VM2) ice loading history and Earth viscosity model[42, 43]. The GIA corrections for the Northern and Southern CAA are 6.8 Gt yr^{-1} and 5.0 Gt yr^{-1}, respectively. Based on a range of realistic viscosity profiles (0.3×10^{21} to 1×10^{21} Pa s and 0.3×10^{21} to 3.6×10^{21} Pa s for the upper and lower mantle, respectively) and alternative loading histories (ICE-3G[56] and the ANU[57] models), we estimate that the GIA correction adds 2.5 Gt yr^{-1} and 4.9 Gt yr^{-1} to the uncertainty of the estimated trend for the Northern and Southern CAA, respectively. GIA adjusted quasi-monthly filtered global GRACE mass anomalies (units of meters water equivalent, relative to August 2003) are provided as Supplementary Data.

Because of the limited spatial resolution of the GRACE data, mass change signals from neighboring regions may leak into the Northern CAA and Southern CAA domains. Variations in ocean mass are removed during the processing of the level-1 satellite data by the GRACE science

team, using the Ocean Model for Circulation and Tides (OMCT)[54]. The residual signal in the ocean shows a trend that is an order of magnitude lower than those in the CAA. The GRACE signal in the Northern CAA and Southern CAA may also be affected by terrestrial water storage variations in adjacent regions. Therefore we simultaneously estimate mass variations in a number of basins in the vicinity of the CAA (Supplementary Fig. 1). The particularly strong mass loss signal of the Greenland Ice Sheet is accounted for by dividing the ice sheet into 16 regions, based on the work of Wouters and others (2008)[29].

Within the Southern CAA and Northern CAA, the GRACE data not allow for a separation between glacier mass changes and mass changes due to changes in the terrestrial water storage. To estimate the potential bias introduced by the latter, we analyzed the output of the Global Land Data Assimilation System (GLDAS)[58] in its NOAH 1° × 1° configuration for each of the GRACE solution CAA domains. Setting contributions from glaciated areas to zero, there are negligible trends in end of the melt season terrestrial water storage of -1.0 ± 3 Gt yr^{-1} and 0.7 ± 11 Gt yr^{-1} for the Northern CAA and Southern CAA respectively. Given the insignificance of the trends in both regions we only include these numbers in our estimates of uncertainty, rather than using them to correct the GRACE data. To reduce the influence of the terrestrial water storage in the glacier mass change signal about 1500 km^2 of the satellite glaciers on Baffin Island (western fringes of the main icefields) are excluded from the GRACE analysis (500 km^2 from R4 and 1000 km^2 from R5: Supplementary Fig. 1). To compensate for the reduced glacier area we scale the final GRACE estimates by the total glacier area divided by the sampled glacier area for each of the respective regions (1.02 for R4 and 1.07 for R5).

In order to assess the performance of our method in recovering mass changes in the North and South CAA, a synthetic model of monthly global surface mass variations spanning the period Apr. 2002 - Aug. 2008 was created. For Greenland, the secular trend was based on a combination of cumulative SMB for the independent RACMO2/GR model, combined with estimates of ice discharge[30, 59]. Variations around the secular trend are taken from the RACMO2/GR model. For non-glaciated areas we use the hydrological GLDAS model[58]. Antarctica has been masked because of the known problems of the GLDAS model in this area and was replaced by GRACE data. Ocean mass variations are modeled under the assumption of a passive ocean, which ensures that mass is conserved within the system[59]. In the Northern and Southern CAA, the GLDAS data are replaced by the RACMO surface mass budget, with a scale factor applied to both regions so that the total linear trend approximately matches those observed by ICESat. The resulting

synthetic surface mass anomaly fields were converted to Stokes coefficients, up to degree and order 60, similar to the GRACE data, and were then used as input for the forward model method. Analysis of the output shows that our method is able to retrieve the trend in the CAA within ±2 Gt yr^{-1}. This indicates that our results for the CAA are not significantly affected by the strong mass loss in the neighboring Greenland Ice Sheet. Determining the change in mass for each of the individual annual mass budget years from monthly GRACE data can prove challenging due to month-to-month noise in the observations and the "retention of meltwater within the glacier drainage system, raise lake levels or percolate into the land subsurface where it will remain stored for some time"[60]. In our analysis we select the annual value to be the most negative mass change occurring at the end of each ablation season (August to September). The full monthly GRACE time series for the Northern CAA and its three subregions are plotted with annual SMB+D and ICESat results in Supplementary Fig. 2 and for the Southern CAA and its two subregions in Supplementary Fig. 3. All subregion time series are included as Supplementary Data. Note that retrieval of mass change from the GRACE signal in the subregions becomes exceedingly more difficult as the impact/influence of noise in the GRACE data increases.

Ice Discharge (*D*)

Published estimates for ice discharge (*D*) from marine-terminating glaciers only exist for the Devon and Agassiz Ice Caps, the Prince of Wales Icefield and the Otto Glacier located on the western end of the Northern Ellesmere Icefields. Outside of these ice masses there is very little information on ice velocities and thicknesses at glacier termini. To estimate the regional mass discharge due to iceberg calving we measured the terminus widths of all tidewater glaciers using 1999-2003 Landsat-7 (ETM+) imagery. For all ice masses with published flux estimates we then determined an average mass discharge per unit terminus width. This value is then multiplied by the remaining terminus widths to derive an estimate of total mass discharge. An uncertainty of 60% is assigned to the average mass discharge per unit terminus width and an uncertainty of 10% is assigned to the terminus widths. Results can be found in Supplementary Table 7. Our estimate of *D* does not include mass change resulting from the advance or retreat of glacier termini. This additional mass change has only a minor impact on sea level change and is not resolved by either ICESat or GRACE.

Supplementary References

31. E. Kalnay *et al.*, The NCEP/NCAR 40-year reanalysis project. *B. Am. Meteorol. Soc.* **77**, 437-471 (1996).

32. S. M. Uppala *et al.*, The ERA-40 re-analysis. *Q. J. Roy. Meteor. Soc.* **131**, 2961-3012 (2005).

33. A. Simmons, S. Uppala, D. Dee, S. Kobayashi, New ECMWF reanalysis products from 1989 onwards. *ECMWF Newsl.* **110**, 29-35 (2007).

34. B. Raup *et al.*, The GLIMS geospatial glacier database: A new tool for studying glacier change. *Global Planet. Change* **56**, 101-110 (2007).

35. D. O. Burgess, M. J. Sharp, Recent changes in areal extent of the Devon Ice Cap, Nunavut, Canada. *Arc. Antarct. Alp. Res.* **36**, 261-271 (2004).

36. J. Brown, O. J. Ferrians, J. A. Heginbottom, E. S. Melnikov, "Circum-Arctic map of permafrost and ground-ice conditions. Boulder, CO: National Snow and Ice Data Center/World Data Center for Glaciology. Digital Media." (1998, revised February 2001).

37. C. S. Ommanney, Canada and the World Glacier Inventory. *Ann. Glaciol.* **50**, 5-10 (2010).

38. E. K. Dowdeswell, J. A. Dowdeswell, F. Cawkwell, On the glaciers of Bylot Island, Nunavut, Arctic Canada. *Arc. Antarct. Alp. Res.* **39**, 402-411 (2007).

39. A. S. Gardner, M. J. Sharp, Sensitivity of net mass balance estimates to near-surface temperature lapse rates when employing the degree-day method to estimate glacier melt. *Ann. Glaciol.* **50**, 80-86 (2009).

40. M. Sharp, L. Copland, K. Filbert, D. Burgess, S. Williamson, in *Glaciological Data Report GD-32, Papers and Recommendations: Snow Watch 2002 Workshop and Workshop on Assessing Global Glacier Recession*. (National Snow and Ice Data Center, Boulder, USA, 2003), pp. 73-75.

41. I. M. Howat, B. E. Smith, I. Joughin, T. A. Scambos, Rates of southeast Greenland ice volume loss from combined ICESat and ASTER observations. *Geophys. Res. Lett.* **35**, L17505 (2008).

42. W. R. Peltier, Global glacial isostasy and the surface of the ice-age Earth: The ICE-5G (VM2) model and GRACE. *Annual Review of Earth and Planetary Sciences* **32**, 111-149 (2004).

43. R. E. M. Riva *et al.*, Glacial isostatic adjustment over Antarctica from combined ICESat and GRACE satellite data. *Earth Planet. Sci. Lett.* **288**, 516-523 (2009).

44. S. A. Khan, J. Wahr, M. Bevis, I. Velicogna, E. Kendrick, Spread of ice mass loss into northwest Greenland observed by GRACE and GPS. *Geophys. Res. Lett.* **37**, L06501 (2010).

45. H. J. Zwally *et al.*, Greenland ice sheet mass balance: distribution of increased mass loss with climate warming; 2003–07 versus 1992–2002. *J. Glaciol.* **57**, 88-102 (2011).

45. J. Wahr, M. Molenaar, F. Bryan, Time variability of the Earth's gravity field: Hydrological and oceanic effects and their possible detection using GRACE. *J. Geophys. Res.* **103**, 30205-30229 (1998).

47. S. Swenson, J. Wahr, Post-processing removal of correlated errors in GRACE data. *Geophys. Res. Lett.* **33**, L08402 (2006).

48. B. Wouters, E. J. O. Schrama, Improved accuracy of GRACE gravity solutions through empirical orthogonal function filtering of spherical harmonics. *Geophys. Res. Lett.* **34**, L23711 (2007).

49. W. M. Kaula, *Theory of satellite geodesy. Applications of satellites to geodesy*. (Waltham, Mass.: Blaisdell Pub Co., 1966, Mineola, NY, USA, 2006), pp. 140

50. K. W. Seo, C. R. Wilson, J. L. Chen, D. E. Waliser, GRACE's spatial aliasing error. *Geophysical Journal International* **172**, 41-48 (2008).

51. B. Wouters, Delft University of Technology (2010).

52. S. Swenson, D. Chambers, J. Wahr, Estimating geocenter variations from a combination of GRACE and ocean model output. *J. Geophys. Res.* **113**, B08410 (2008).

53. M. K. Cheng, B. D. Tapley, Variations in the Earth's oblateness during the past 28 years. *J. Geophys. Res.* **109**, B09402 (2004).

54. F. Flechtner, AOD1B Product Description Document for Product Releases 01 to 04. *University of Texas at Austin, GRACE 327-750, CSR Publ. GR-GFZ-AOD-0001 Rev. 3.1*, 1-43 (2007).

55. R. Kistler *et al.*, The NCEP-NCAR 50-year reanalysis: Monthly means CD-ROM and documentation. *B. Am. Meteorol. Soc.* **82**, 247-267 (2001).

56. A. M. Tushingham, W. R. Peltier, IIce-3G: A New Global Model Of Late Pleistocene Deglaciation Based Upon Geophysical Predictions Of Post-Glacial Relative Sea Level Change *J. Geophys. Res.* **96**, 4497-4523 (1991).

57. K. Lambeck, F. Antonioli, A. Purcell, S. Silenzi, Sea-level change along the Italian coast for the past 10,000 yr. *Quaternary Sci. Rev.* **23**, 1567-1598 (2004).

58. M. Rodell *et al.*, The global land data assimilation system. *B. Am. Meteorol. Soc.* **85**, 381-394 (2004).

59. J. Ettema *et al.*, Higher surface mass balance of the Greenland ice sheet revealed by high-resolution climate modeling. *Geophys. Res. Lett.* **36**, (2009).

60. A. A. Arendt, S. B. Luthcke, R. Hock, Glacier changes in Alaska: Can mass-balance models explain GRACE mascon trends? *Ann. Glaciol.* **50**, 148-154 (2009).

61. D. R. Mueller, W. F. Vincent, Microbial habitat dynamics and ablation control on the Ward Hunt Ice Shelf. *Hydrol. Process.* **20**, 857-876 (2006).

62. D. A. Fisher, R. M. Koerner, Signal and noise in four ice-core records from the Agassiz Ice Cap, Ellesmere Island, Canada: Details of the last millennium for stable isotopes, melt and solid conductivity. *The Holocene* **4**, 113-120 (1994).

63. R. Koerner, Accumulation, ablation, and oxygen isotope variations on the Queen Elizabeth Islands ice caps, Canada. *J. Glaciol.* **22**, 25-41 (1979).

64. E. Mekis, W. D. Hogg, Rehabilitation and analysis of Canadian daily precipitation time series. *Atmos. Ocean* **37**, 53-85 (1999).

65. R. M. Koerner, Accumulation on the Devon Island Ice Cap, Northwest Territories, Canada. *J. Glaciol.* **6**, 383-392 (1966).

66. W. Colgan, M. Sharp, Combined oceanic and atmospheric influences on net accumulation on Devon Ice Cap, Nunavut, Canada. *J. Glaciol.* **54**, 28-40 (2008).

67. D. Mair, D. Burgess, M. Sharp, Thirty-seven year mass balance of Devon Ice Cap, Nunavut, Canada, determined by shallow ice coring and melt modeling. *J. Geophys. Res.* **110**, F01011 (2005).

68. G. Hattersley-Smith, Climatic inferences from firn studies in northern Ellesmere Island. *Geografiska Annaler* **45**, 139-151 (1963).

69. K. C. Arnold, thesis, McGill University (1968).

70. F. Müller, B. Stauffer, G. Schriber, paper presented at the Isotopes and impurities in snow and ice symposium, Grenoble, France, Aug.-Sept. 1975, 188-196 (1975).

71. F. Müller, "Investigations in an ice shaft in the accumulation area of the McGill Ice Cap" (Axel Heiberg Island Research Reports, 27-36. McGill University, Montréal, Québec, 1963).

72. I. Koch, thesis, University of Alberta (2009).

73. D. Mair *et al.*, Mass balance of the Prince of Wales Icefield, Ellesmere Island, Nunavut, Canada. *J. Geophys. Res.* **114**, F02011 (2009).

74. C. Braun, D. R. Hardy, R. S. Bradley, V. Sahanatien, Surface mass balance of the Ward Hunt Ice Rise and Ward Hunt Ice Shelf, Ellesmere Island, Nunavut, Canada. *J. Geophys. Res.* **109**, D22110 (2004).

75. R. J. Braithwaite, Y. Zhang, Sensitivity of mass balance of five Swiss glaciers to temperature changes assessed by tuning a degree-day model. *J. Glaciol.* **46**, 7-14 (2000).

76. A. A. Arendt, K. A. Echelmeyer, W. D. Harrison, C. S. Lingle, V. B. Valentine, Rapid wastage of Alaska glaciers and their contribution to rising sea level. *Science* **297**, 382-386 (2002).

77. C. Nuth, G. Moholdt, J. Kohler, J. O. Hagen, A. Kääb, Svalbard glacier elevation changes and contribution to sea level rise. *J. Geophys. Res.* **115**, F01008 (2010).

78. S. Williamson, M. Sharp, J. Dowdeswell, T. Benham, Iceberg calving rates from northern Ellesmere Island ice caps, Canadian Arctic, 1999-2003. *J. Glaciol.* **54**, 391-400 (2008).

79. D. O. Burgess, M. J. Sharp, D. W. F. Mair, J. A. Dowdeswell, T. J. Benham, Flow dynamics and iceberg calving rates of Devon Ice Cap, Nunavut, Canada. *J. Glaciol.* **51**, 219-230 (2005).

80. J. G. Cogley, W. P. Adams, M. A. Ecclestone, F. Jung-Rothenhäusler, C. S. L. Ommanney, Eds., *Mass balance of Axel Heiberg Island glaciers, 1960–1991: a reassessment and discussion.*, (Environment Canada. National Hydrology Research Institute, Saskatoon, Sask., 1995).

81. C. Braun, D. R. Hardy, R. S. Bradley, Mass balance and area changes of four High Arctic plateau ice caps, 1959-2002. *Geog. Ann. A* **86**, 43-52 (2004).

Supplementary Tables

Supplementary Table 1: Mean elevation bias, standard deviation (σ) and percentage outliers (iterative 3σ edit at 5 % convergence) of the ASTER GDEM and CDED DEMs with respect to ICESat fall 2003 observations over land and glacier surfaces in Northern CAA and Southern CAA. Based on these results, the ASTER GDEM was adjusted for a mean bias of -14 m, while no corrections were applied to the CDED DEM.

		GDEM - ICESat			CDED - ICESat		
Region	Nr. of obs.	Bias (m)	σ (m)	Outliers (%)	Bias (m)	σ (m)	Outliers (%)
NCAA land	134076	-13.5	26.2	4.3	-5.6	43.1	2.3
NCCA glacier	100793	-14.2	19.0	4.8	0.1	45.6	2.0
SCAA land	56725	-14.2	21.6	6.7	-2.3	26.2	4.4
SCAA glacier	14383	-15.4	29.6	6.5	10.2	37.6	2.5

Supplementary Table 2: On-ice temperature measurements used for the bias-correction of NCEP/NCAR R1 monthly averages and standard deviations in temperature.

	Lat (°N)	Lon (°E)	Elev. (m MSL)	Years	Source
Agassiz Ice Cap*	80.80	-72.90	1736	Jun 1988 - Apr 2009	[20]
Devon Ice Cap*	75.34	-82.10	1880	Apr 1997 - May 2009	[20]
Meighen Ice Cap	79.96	-99.14	250	Apr 2004 - Apr 2009	[7]
Prince of Wales*	78.49	-79.43	1727	May 2001 - Apr 2003	[20]
Ward Hunt Ice Shelf	83.08	-74.42	3	Aug 2001 - Jul 2003	[61]

* Daily summit temperature generated by extrapolating measurements made along elevation transect.

Supplementary Table 3: Precipitation records used for the bias-correction of NCEP/NCAR R1 average annual precipitation.

	Precip. (kg m^{-2} yr^{-1})	Lat (°N)	Lon (°E)	Elev. (m)	Years	Missing years	Source	Notes
Agassiz N a	147	80.70	-73.10	1700	1948-1988		[62]	
Agassiz N b	180	80.72	-73.6*	1827	1963-1973		[63]	
Agassiz NE	300*	80.20*	-70.50*	0*	1963-1973		[63]	
Agassiz S	330	80.05	-77.50*	1754	1963-1973		[63]	
Agassiz SW	150*	80.00*	-80.00*	1050*	1963-1973		[63]	
Alert	220	82.51	-62.27	31	1951-1999		[64]	N1
Devon SE	568*	74.90*	-81.25*	750*	1962-1965	1	[65]	N2
Devon S	269*	75.00*	-82.83*	850*	1962-1965	1	[65]	N2
Devon C	242	75.34	-82.68	1825	1963-2003		[66]	
Devon C1	241	75.31	-82.14	1930	1963-2000		[67]	
Devon NW	167*	75.52*	-83.10*	1000*	1962-1965	1	[65]	N2
Devon D	174	75.51	-82.27	1525	1963-2003		[66]	
Devon C4	159	75.42	-82.95	1640	1963-2000		[67]	
Devon C5	138	75.49	-82.60	1508	1963-2000		[67]	
Devon E	234	75.19	-82.37	1525	1963-2003		[66]	
Devon B	223	75.34	-83.17	1630	1963-2003		[66]	
Devon C7	159	75.21	-82.84	1504	1963-2000		[67]	
Ellesmere N	158	82.28*	-72.65*	1660	1948-1961		[68]	
Eureka	110	79.97	-85.92	10	1948-2006	1	[64]	N1
Gilman	173	82.17	-72.69	1660	1957-1966		[69]	
Grant	200*	81.50*	-81.00*	1700*	1963-1973		[63]	
Grise	187	76.42	-82.90	45	1991-2006	4	[64]	N1
Manson a	564	76.64	-79.50	903	1963-1973		[70]	N3
Manson b	998	76.63	-78.37	660	1967-1974		[63]	N4
Meighen	281	79.96	-99.14	250	1961-2008	4	[7]	N2
Muller a	288	79.93	-91.90	1920	1948-1961		[71]	
Muller b	160	79.77	-91.3*	1810	1963-1973		[63]	
POW N a	307	78.49	-79.43	1727	1966-1999		[72]	
POW N b	320	78.57	-79.60*	1696	1963-1973		[63]	
POW NE	273	78.70	-77.40	1419	1963-2000		[73]	
POW S a	394	77.87	-80.81	1350	1975-2000		[72]	
POW S b	572	78	-80.33	1350	1956-1974		[70]	
Resolute	230	74.72	-94.98	67	1948-2006		[64]	N1
Sydkap	370	76.86	-86.00*	1433	1963-1973		[63]	
Ward Hunt a	288	83.13	-74.10	20	1959-1989	10	[74]	N2
Ward Hunt b	243	83.09	-73.78	2	1967-1989	7	[74]	N2

* Estimated from published diagram.

N1 Adjusted Historical Canadian Climate Data (AHCD) available from Environment Canada, N2 winter values multiplied by 1.6 to account for summer precip. (estimated form AHCD stations), N3 scaled by 1.4 to account for mass loss due to runoff (estimated from model), N4 scaled by 1.2 to account for mass loss due to runoff (estimated from model).

Supplementary Table 4: Model free variable assignment.

Free variable	Mean ± 1σ	Units	Source	Notes
Mean summer temperature lapse rate	4.9 ± 0.9	°C km^{-1}	[20]	
Sensitivity of lapse rate to anomalies in temperatures	-1.1 ± 0.3	°C km^{-1}	[20]	
Degree day factor for snow	4.7 ± 1.5	kg m^{-2} d^{-1} °C^{-1}	[75, 18]	N1
Degree day factor for ice	8.1 ± 2.6	kg m^{-2} d^{-1} °C^{-1}	[75, 18]	N1
Precipitation uncertainty	0 ± 33	%		N2

N1 duplicates and outliers (> 2σ) removed, N2 standard error between corrected reanalysis precipitation and observations

Supplementary Table 5: Regional area-averaged annual elevation change (*dh/dt*) estimates for 2003-2009 determined using a range of extrapolation methods: median *dh/dt*, mean *dh/dt*, hypsometric median *dh/dt* [9], hypsometric mean *dh/dt* [76], hypsometric 3rd-5th order polynomial fits to *dh/dt* [77].

Glacier region	Area (km^2)	Median (m yr^{-1})	Mean (m yr^{-1})	Median bin (m yr^{-1})	Mean bin (m yr^{-1})	3rd pol. (m yr^{-1})	4th pol. (m yr^{-1})	5th pol. (m yr^{-1})
NCAA	106400	-0.29	-0.37	-0.35	-0.38	-0.38	-0.38	-0.38
SCAA	42000	-0.70	-0.70	-0.69	-0.69	-0.69	-0.69	-0.69
NCAA tidewater	48000	-0.28	-0.37	-0.34	-0.37	-0.37	-0.37	-0.37
NCAA land-term.	58400	-0.29	-0.37	-0.36	-0.39	-0.39	-0.39	-0.39
NCAA sum	106400	-0.29	-0.37	-0.35	-0.38	-0.38	-0.38	-0.38
NCAA R1	49700	-0.22	-0.30	-0.27	-0.30	-0.30	-0.30	-0.30
NCAA R2	12000	-0.50	-0.56	-0.54	-0.55	-0.55	-0.54	-0.55
NCAA R3	44700	-0.38	-0.45	-0.43	-0.45	-0.45	-0.45	-0.45
NCAA sum	106400	-0.32	-0.39	-0.37	-0.39	-0.39	-0.39	-0.39
SCAA R4	28200	-0.73	-0.71	-0.69	-0.69	-0.69	-0.69	-0.69
SCAA R5	13800	-0.62	-0.68	-0.77	-0.74	-0.71	-0.71	-0.71
SCAA sum	42000	-0.69	-0.70	-0.72	-0.71	-0.70	-0.70	-0.70

Supplementary Table 6: Estimate of dynamic mass flux (*D*).

Ice Mass/Region	Total Width (km)	Uncertainty (km)	Flux (Gt yr^{-1})	Uncertainty (Gt yr^{-1})
Agassiz Ice Cap [78]	38	3.8	0.41	0.08
Devon Island Ice Cap [79]	84	8.4	0.38	0.13
Prince of Wales Icefield [73]	194	19.4	1.49	0.19
Otto Glacier, N. Ellesmere [78]	5	0.5	0.23	0.05
North CAA Known	321	32.1	2.51	0.45
Axel Heiberg Island	4	0.4	unknown	unknown
Devon Island Icefields	6	0.6	unknown	unknown
Sydkap Ice Cap	7	0.7	unknown	unknown
Coburg Island	15	1.5	unknown	unknown
N. Ellesmere Ice Caps	106	10.6	unknown	unknown
Manson Ice Cap	132	13.2	unknown	unknown
North CAA estimate	269	26.9	2.10	1.47
Baffin Island	28	2.8	unknown	unknown
Bylot Island	4	0.4	unknown	unknown
South CAA estimate	32	3.2	0.25	0.18
Total	622	62.2	4.86	2.10

Supplementary Table 7: *In situ* measurements of glacier surface mass budget.

	Lat (°N)	Lon (°E)	Elev. (m)	Years	Missing years	Source
Agassiz Ice Cap - N‡	80.87	-71.30	435 - 1315	1977-2008	2	[7]
Baby Glacier*	79.43	-90.67	1007	1960-2003	14	[80]
Devon Ice Cap - NW‡	75.65	-83.19	100 - 1815	1961-2008		[7]
Meighen Ice Cap‡	79.99	-99.16	85 - 267	1963-2008	11	[7]
Murray Ice Cap*	81.33	-69.23	1080	1999-2002		[81]
Simmons Ice Cap*	81.29	-68.90	1020	2000-2001		[81]
St. Patrick Bay ice cap - NE*	81.93	-64.17	840	1972-1983	5	[81]
St. Patrick Bay ice cap - SW*	81.93	-64.49	780	1980		[81]
Ward Hunt Ice Rise*	83.13	-74.10	20	1959-2003	27	[74]
Ward Hunt Ice Sheet*	83.09	-73.78	20	1967-1985	8	[74]
White Glacier	79.48	-90.77	98 - 1521	1983-2008	3	[80]

*Integrated glacier annual value for entire ice mass because of small area. ‡Dataset provided by the Geological Survey of Canada.

Supplementary Figures and Legends

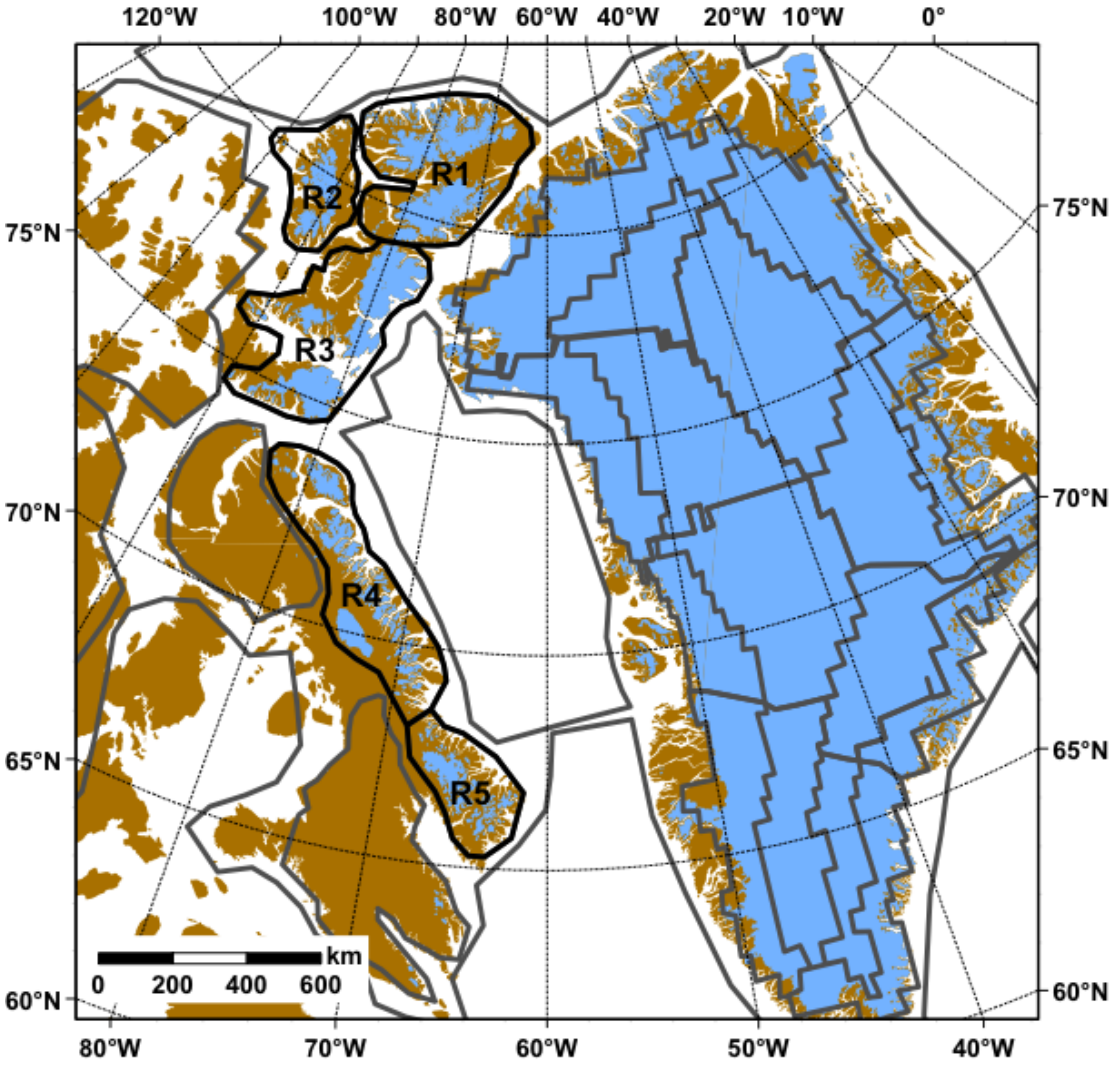

Supplementary Figure 1: Map showing the pre-defined basins used in the forward method to estimate mass anomalies from the GRACE data in the Northern CAA (R1-R3) and Southern CAA (R4-R5). Similar boundaries were used to derive subregion mass changes from the surface mass budget model and ICESat datasets (See Supplementary Fig. 2 and 3). Mass anomalies were simultaneously estimated in the surrounding regions to account for leakage due to the limited spatial resolution of the GRACE observations.

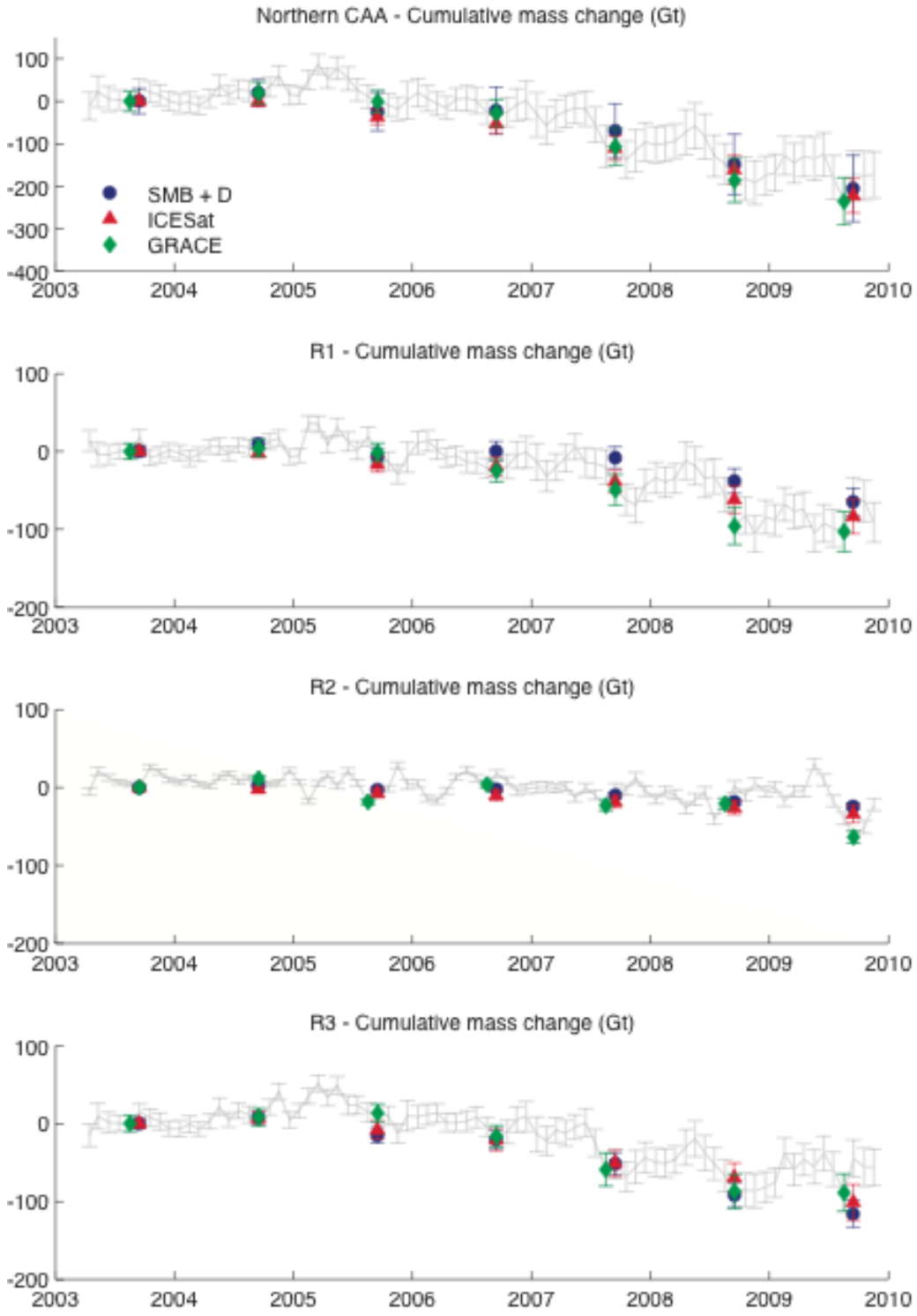

Supplementary Figure 2: Regional breakdown of cumulative mass change in the Northern CAA (mean ± 2σ). Monthly GRACE results shown in grey. Winter GRACE results represents mass accumulation on glaciers plus the surrounding land surfaces. See Supplementary Fig. 1 for map showing region boundaries.

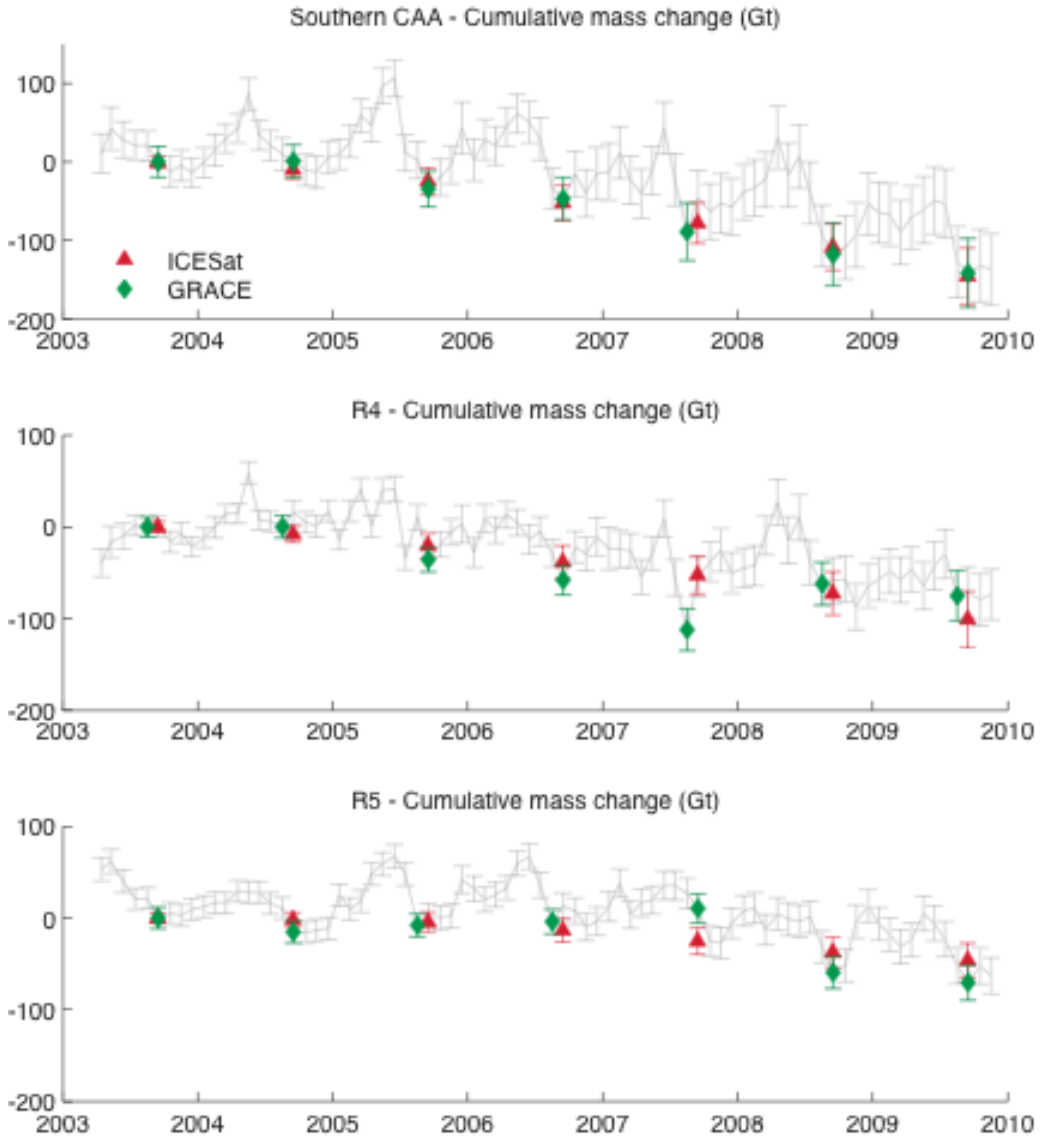

Supplementary Figure 3: Regional breakdown of cumulative mass change in the Southern CAA (mean ± 2σ). Monthly GRACE results shown in grey. Winter GRACE results represents mass accumulation on glaciers plus the surrounding land surfaces. See Supplementary Fig. 1 for map showing region boundaries.

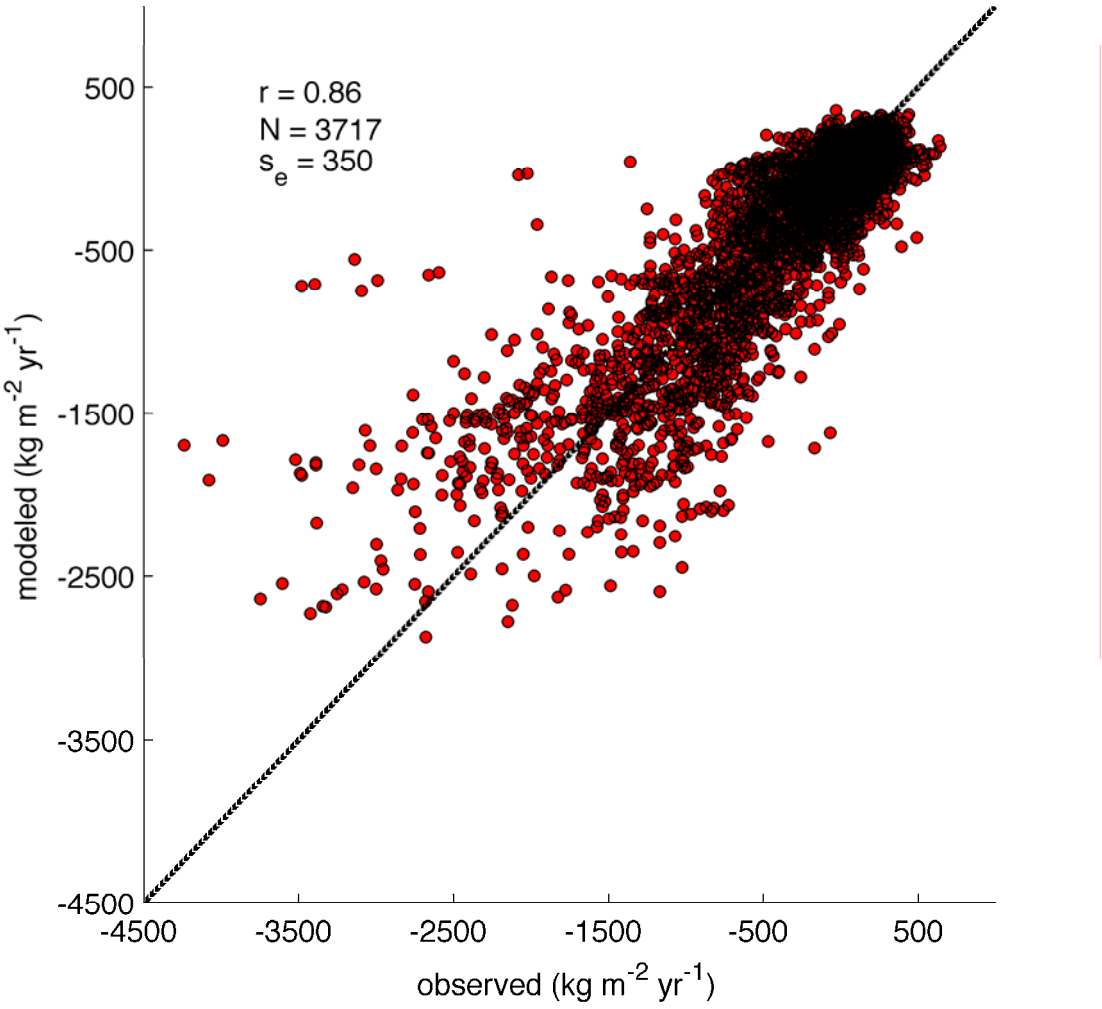

Supplementary Figure 4: Modeled versus measured annual surface mass budget at point locations. See Supplementary Table 7 for details on observation values. Model performance is poorest near the glacier margins where the surface mass budgets are most negative and have the largest spatial and interannual variability. Northern CAA point location surface mass balance measurements collected between 1950 and 2008 are included as Supplementary Data.

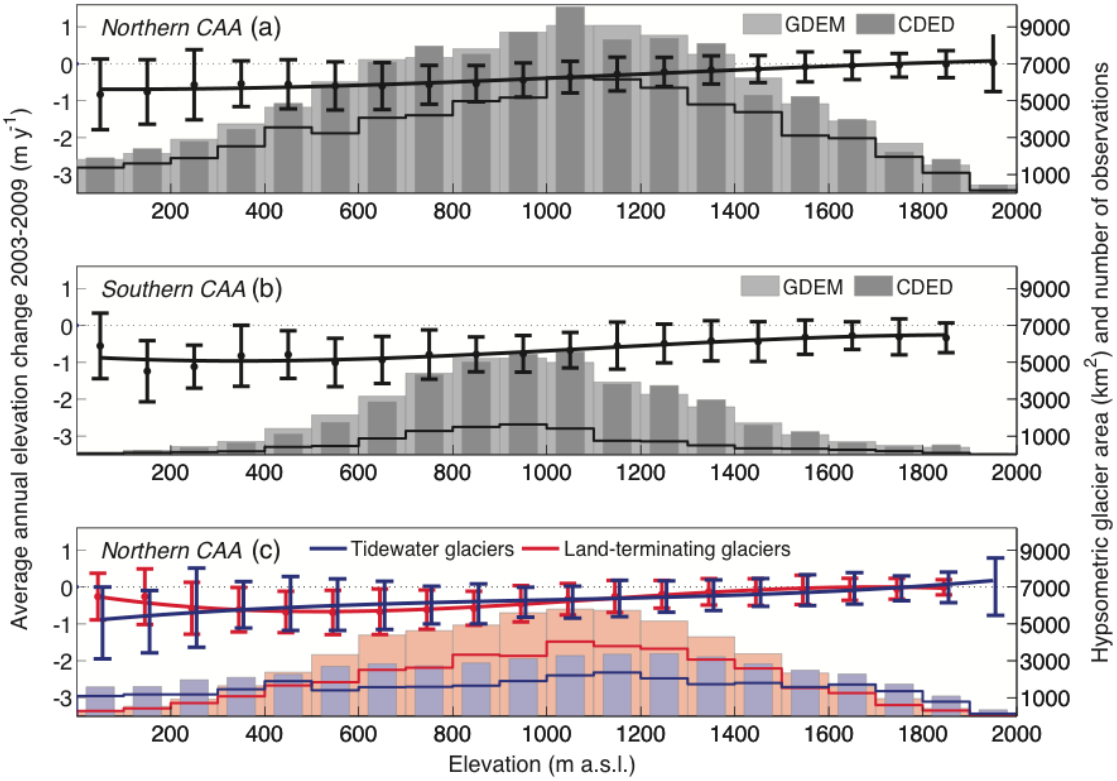

Supplementary Figure 5: Third order polynomial curves fitted to average annual elevation changes (*dh/dt*) between fall 2003 and fall 2009 in (a) Northern CAA, (b) Southern CAA, and (c) Northern CAA with a separation between tidewater and land-terminating glacier basins. Dots and error bars show the mean and standard deviation of *dh/dt* within 100 m elevation bins. The glacier area of each bin is shown with filled bars for (a-c) the ASTER GDEM and (a-b) the CDED DEM. The unfilled bars represent the number of *dh/dt* observations per bin, multiplied by 2 for scaling. The decreased magnitude of the *dh/dt* values at low elevations is an artifact of increased sampling of non-ice areas, which results from glacier retreat and/or inaccurate outlines. This is particularly evident for Southern CAA and land-terminating of the Northern CAA. Sampling of bedrock has minimal impact on total volume and mass change estimates (see text).

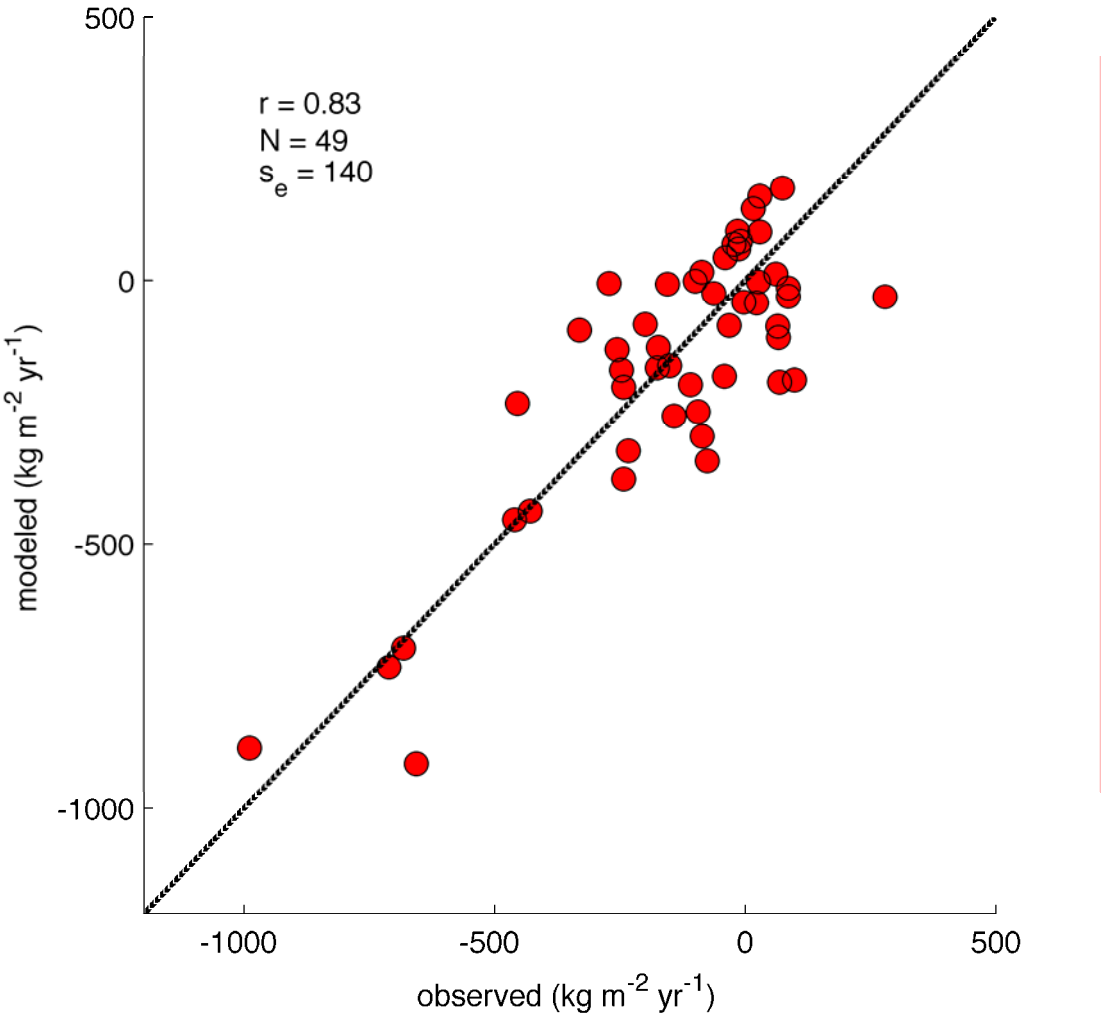

Supplementary Figure 6: Modeled versus measured annual average of basin-integrated surface mass budget. See text for details.

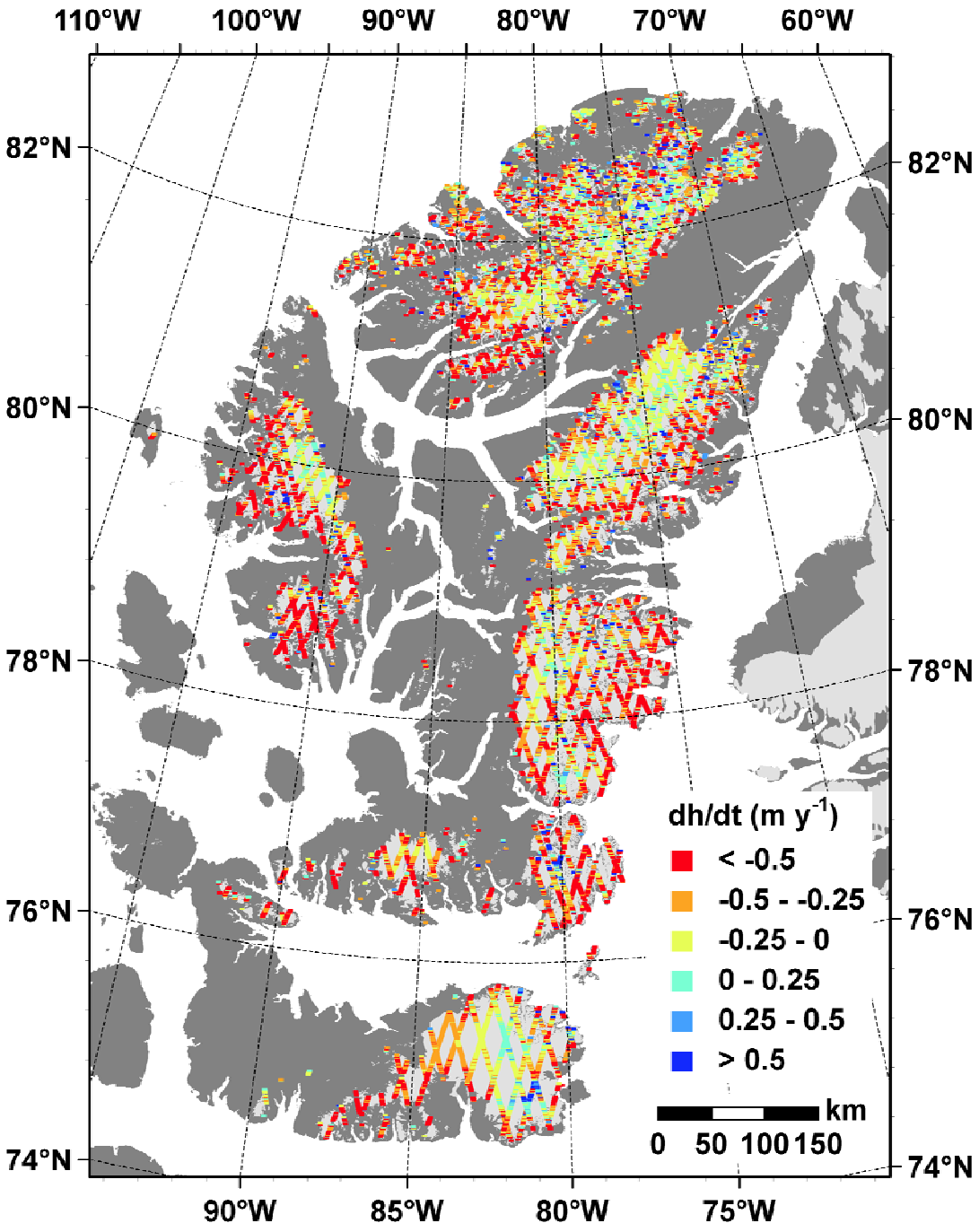

Supplementary Figure 7: Average annual elevation changes *dh/dt* between fall 2003 and fall 2009 in the Northern CAA. There are 34800 *dh/dt* observations over a glacier area of 106400 km^2, yielding a hypsometrically area-averaged *dh/dt* of -0.38 ± 0.04 m yr^{-1}.

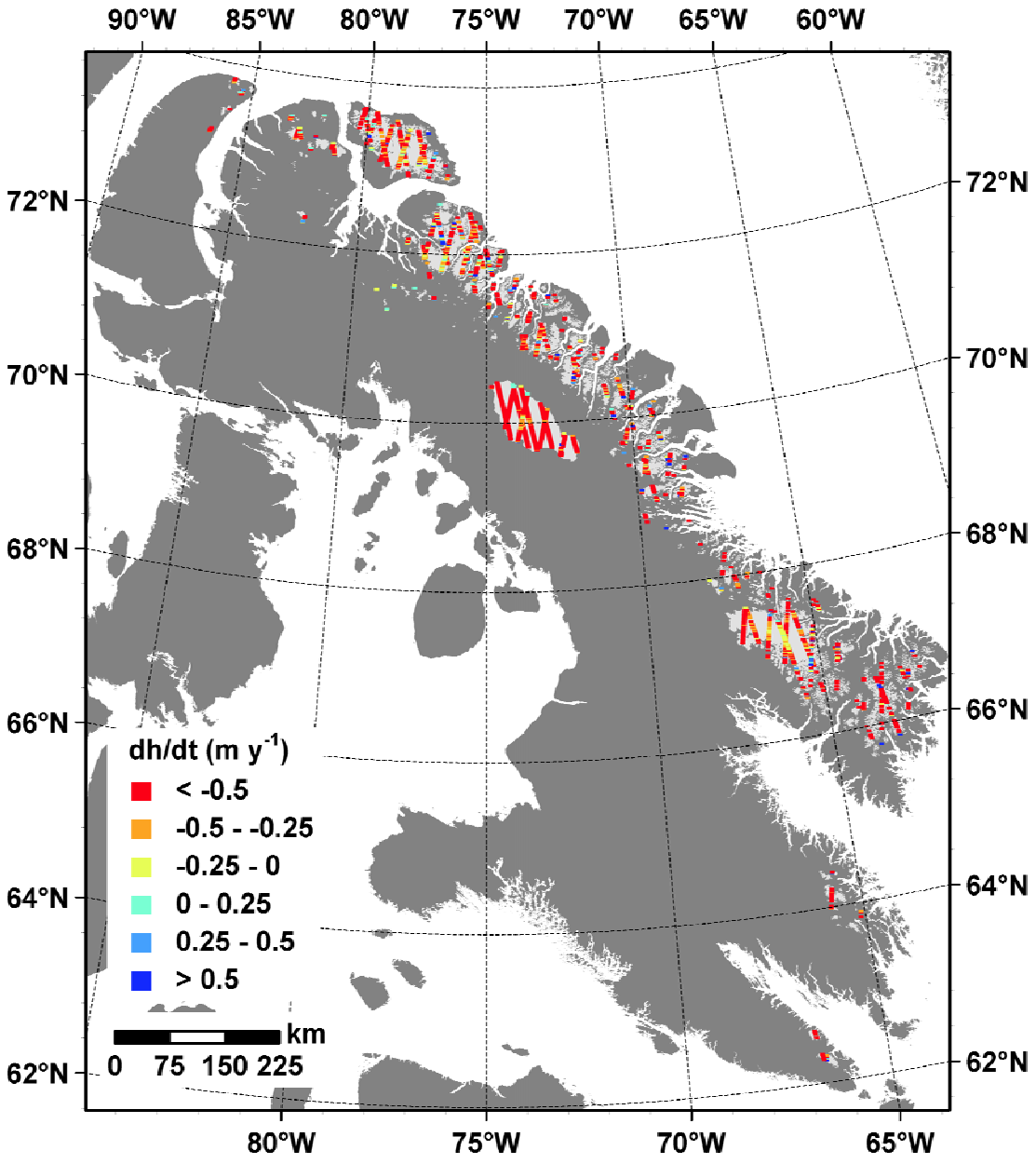

Supplementary Figure 8: Average annual elevation changes (*dh/dt*) between fall 2003 and fall 2009 in the Southern CAA. There are 5600 *dh/dt* observations over a glacier area of 42000 km^2, yielding a hypsometrically area-averaged *dh/dt* of -0.69 ± 0.09 m yr^{-1}.